Controlled Growth from ZnS Nanoparticles to ZnS–CdS Nanoparticle Hybrids with Enhanced Photoactivity

*Xiaojie Xu, Linfeng Hu, Nan Gao, Shaoxiong Liu, Swelm Wageh, Ahmed A. Al-Ghamdi, Ahmed Alshahrie, and Xiaosheng Fang**

Chalcogenide nanostructures and nanocomposites have been the focus of semiconductor nanomaterial research due to their remarkable optoelectronic and photocatalytic properties and potential application in photodegrading enviromental pollutions. However, currently available synthesizing methods tend to be costly and inefficient. In this paper, we propose a facile two-step solution-phase method to synthesize well-defined monodisperse ZnS–CdS nanocomposites. The morphology and size of ZnS nanoparticles can be easily controlled by adjusting the amount of the source of sulfur. After surface modification with tiny CdS nanoparticles through natural electrostatic attraction, uniform ZnS–CdS nanocomposites are obtained, which has been further confirmed by transmission electron microscopy (TEM) and energy dispersive spectrometry (EDS). The photocatalytic activities of various ZnS samples and ZnS–CdS nanocomposites have been investigated by degrading Rhodamine B under UV-light. Compared with pure ZnS nanoparticles and ZnS powders, the as-obtained ZnS–CdS nanocomposites exhibit excellent photocatalytic performances due to the effective charge separation and increased specific surface area by the attachment of CdS. Moreover, resulting from the effective passivation of surface electronic states, the photoluminescence intensity of the ZnS–CdS nanocomposites is also significantly improved relative to plain ZnS.

1. Introduction

Semiconductor nanomaterials have attracted worldwide attention due to their unique optoelectronic properties suitable for applications in gas sensors, UV detectors, photovoltaic devices, and photocatalysis.[1–3] Particularly, metal sulfide semiconductors, such as ZnS,[4] have been the focus of scientific research in recent years because of its versatile fundamental properties for diverse applications.[5] Morever, with the growing concerns over environmental pollution, the importance of such inorganic nanomaterials has been increasingly noticed due to their potential applications in photocatalytic activities, especially in photodegradation of organic pollutants and hydrogen production through water splitting.[6]

Therefore, in the past few decades, great efforts have been steadily spent to develop ZnS nanostructures, aiming to enhance their photocatalytic performance via specific surface enlargement and effective charge seperation. For example, Zhang et al.[7] reported the preparation of ZnS nano-architectures composed of interwoven nanosheets which show a complete degradative process of Eosin B within 60 min. Qian et al.[6a] tuned the morphology and size of ZnS nanoparticles (NPs) by varying the reaction time and volume ratio of mixed solutions to improve the photocatalytic performance. Besides, Mohammadikish et al.[8] proposed a hydrothermal route for preparation of solid and hollow ZnS nanostructures through adjusting the amount of the source of sulfur. However, the majority of the reported ZnS photocatalysts still suffer from a relatively low photodecomposition efficiency, because of the fairly large band gap of ZnS (≈3.7 eV at 300 K), which leads to inefficient use of solar energy.[9] In addition, the high-cost and complicated preparation routes also put an impediment in the way of applying ZnS catalysts.

A promising approach to improve the photocatalytic activities is to exploit well-defined heterostructures. It has been demonstrated that dual semiconductor nanocomposites (NCs) often exhibit superior properities or new features compared with the individual constituent alone, due to the coupling effects that can induce significant enhancement in a few areas, including charge seperation, transportation and prolonged lifetime of charge carriers.[10] Likewise, the matching of band gaps between the two components of the semiconductor NCs, such as CdS/ZnS,[11] CdSe/ZnS,[12] CdSe/CdS,[13] and ZnO/ZnS,[14] has been critically concerned to improve the charge transfer efficiency. With a band gap energy of ≈2.4 eV at 300 K, CdS plays a significant role in the photocatalytic field resulting from the well-matched photoresponse region of sunlight, relatively low function, excellent transportation, and high electronic mobility.[15] For example, Zhan et al.[16] synthesized one-dimensional CdS/ZnS core–shell NCs via a two-step solvothermal method. The reported CdS/ZnS sample exhibited a double photocatalytic rate as that of pure CdS nanowires in the degradation of

X. J. Xu, Prof. L. F. Hu, Dr. N. Gao, Dr. S. X. Liu, Prof. X. S. Fang
Department of Materials Science
Fudan University
Shanghai 200433, P. R. China
E-mail: xshfang@fudan.edu.cn
Dr. S. Wageh, Dr. A. A. Al-Ghamdi, Dr. A. Alshahrie, Prof. X. S. Fang
Department of Physics
Faculty of Science
King Abdulaziz University
Jeddah 21589, Saudi Arabia

DOI: 10.1002/adfm.201403065

Methylene Blue under visible light. Lin et al.[17] developed a unique route for the growth of coaxial CdS/ZnS nanowires by a one-step metal-organic chemical deposition method and noticed the great rise in photoluminescence (PL) intensity of the coaxial nanowires, relative to that of each component. Liu et al.[18] reported the preparation of urchin-like micro-scaled ZnS/CdS composites by combining a solvothermal route with the precipitation process and observed that 80% degradation of Rhodamine B could be achieved within 75 min. On the other hand, the counterparts of CdS/ZnS NCs, namely the ZnS/CdS NCs, are yet to be studied commensurately. In fact, the development of new heterostructures still remains a challenge for scientific research in terms of several critical factors, such as the comportable lattice interface, the enhancement of total activation site, and the facile preparation.[9]

In this study, we propose a straightfoward method to synthesize spherical ZnS/CdS NCs via a two-step solution-phase route. To the best of our knowledge, it is the first systematical report of the successful preparation of monodisperse zero-dimensional ZnS/CdS NCs with high productivity. More importantly, the as-obtained products exhibit great enhancement of photodegradation efficiency and PL intensity with respect to the individual constituents due to the effective separation of photogenerated electrons and holes.[19] Tunable synthesis of various ZnS cores is also investigated in this work, and monodisperse ZnS nanoparticles (NPs) with different sizes and surface roughness can be obtained by altering the S source quantity in the aqueous solution. Afterwards, the as-acquired ZnS cores are decorated with tiny CdS NPs through a simple chemical precipitation process. The photocatalytic efficiency of the CdS-functionalised ZnS catalysts towards Rhodamine B is about three times as much as that of pure ZnS cores. This straightforward and low-cost method provides the flexibility of synthesizing and testing a wide spectrum of different NCs ratios at very low cost and high throughput rate, and thus would greatly enable researchers to investigate and optimize the dual-semiconductor material system and accelerating the translation into applications in photocatalysts, and other photovoltaic devices.

2. Results and Discussions

2.1. Structure and Morphology Analysis

2.1.1. ZnS Nanoparticles

To verify the purity and crystallinity of the ZnS NPs prepared at different starting ratios of Zn source to S source, we performed an X-ray diffraction on the synthesized samples. **Figure 1** shows the X-ray diffraction (XRD) patterns of ZnS nanoparticles (NPs) prepared at different molar ratios of the Zn source ($Zn(AC)_2$) against the S source (CH_3CSNH_2, TAA) with the assistance of surfactant PVP at 100 °C for 2 h. All the diffraction peaks of ZnS NPs can be indexed as blende ZnS (cubic β-ZnS structure) with lattice constants of a = 5.345 Å (JCPDS Card No. 80–0020). No other peaks of impurities were observed, suggesting the high purity of the as-synthesized products. As can be seen from Figure 1, when increasing the amount of TAA within a certain range, the crystallinity of as-obtained ZnS also increased. In particular, the ZnS sample prepared at the starting ratio of

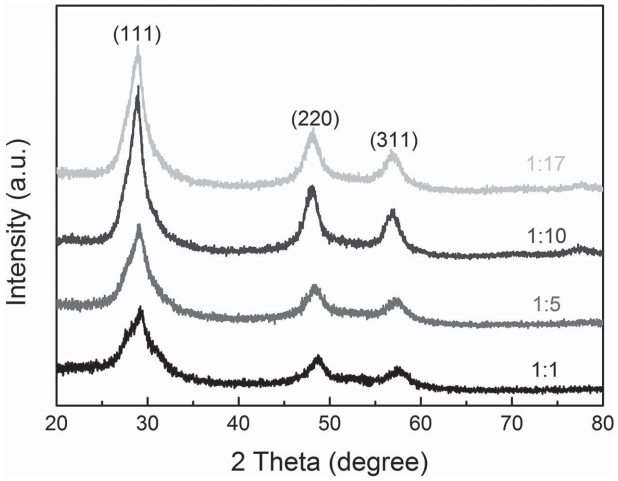

Figure 1. XRD patterns of pure ZnS NPs obtained at different molar ratios of $Zn(Ac)_2$ to TAA: 1:1, 1:5, 1:10, 1:17 (as indicated), with the reaction time of 2 h at 100 °C.

$C_{Zn(Ac)2}$:C_{TAA} = 1:10 displayed the highest crystallinity, on which the following study was focused. Moreover, it's noticeable that the peaks gradually narrowed with the increase in S souce, indicating that average crystallite sizes were growing larger according to Scherrer's Equation below:

$$D = \frac{K\lambda}{\beta \cos\theta}$$

where D is the mean diameter of the crystallite, K is a constant related to the dimensionless shape (where k = 0.89 in this case), λ is the wavelength of X-ray (where Cu Kα = 0.154178 nm), β is the full width half maximum of the intensity (FWHM), and θ is the corresponding Bragg angle. The results are summarized in **Table 1**, and it is clear to see that crystals tended to grow bigger at higher concentration of TAA, which is ascribed to the increasing release rate of S^{2-}. As smaller crystallinites might induce more crystal lattice imperfections, such as dislocations and stacking faults,[20] the ZnS samples prepared at lower level of TAA display poorer crystallinity.

The morphology and structure of the as-synthesized ZnS NPs were investigated using field-emission scanning electron microscopy (FESEM) and transmission electron microscopy (TEM). As depicted in the SEM images of **Figure 2**, the coarse surface indicates that ZnS NPs were formed of self-aggregated tiny ZnS NPs, driven by electrostatic gravitation and surface

Table 1. Comparison of average crystallite sizes of pure ZnS NPs obtained at different molar ratios of $Zn(Ac)_2$ to TAA, 1:1, 1:5, 1:10, and 1:17, respectively, from the XRD patterns.

Sample	β [°] (FWHM) (1 1 1)	Mean crystal size [nm]
ZnS (1:1)	3.108	≈2.89
ZnS (1:5)	2.767	≈3.25
ZnS (1:10)	1.860	≈4.83
ZnS (1:17)	2.036	≈4.41

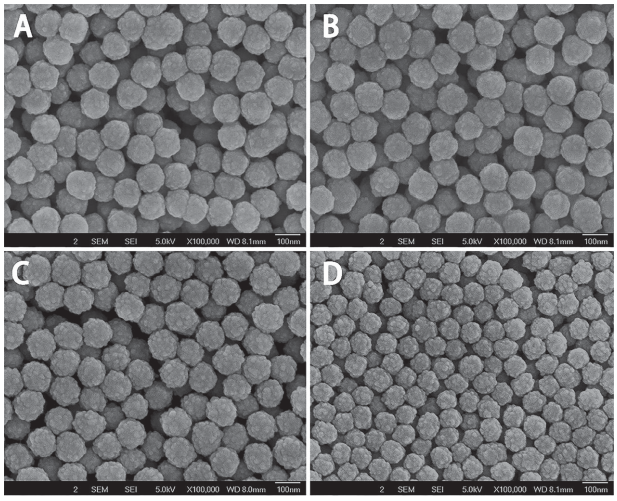

Figure 2. SEM images of pure ZnS NPs synthesized at different molar ratios of $Zn(Ac)_2$ to TAA at 100 °C for 2 h: A)1:1, B)1:5, C)1:10, and D)1:17, respectively.

energy minimization.[21] It is also noticed that the ZnS samples prepared with the assistance of surfactant PVP were uniform and well-dispersed in spite of the different starting ratios of the Zn source against the S source. Interestingly, the surface morphology of ZnS NPs became rougher with the increase in the S source. The increasing crystal sizes along with the S quantity as discussed in XRD pattern were responsible for the coarsening process. Moreover, the mean sizes of ZnS NPs were slightly varied, reaching a noticeable difference at the starting ratio of $C_{Zn(Ac)2}$:C_{TAA}= 1:17, which is attributed to the restraint effect caused by excess TAA absorbed on the surface of ZnS NPs.[15]

The corresponding TEM images in **Figure 3** further confirm that the spherical structures of ZnS were assemblies of numerous tiny particles. A closer examination of the edges of the products suggests a tendency for coarseness, which is consistent with the result above. To further investigate the effect of size differences, the particle size distributions were obtained from TEM images of more than 500 representative nanoparticles for each sample with microscopic measurement. As can be seen from the insets of Figure 3, the narrow distribution of particle sizes suggests the uniformity of the as-prepared ZnS samples. It is also noticed that, as the starting ratios of $Zn(Ac)_2$ to TAA increased, the average diameters of ZnS NPs gradually decreased, indicating the important role TAA played in the formation process of ZnS NPs. In fact, TAA hydrolyzed in aqueous solution and released S^{2-} by breaking the C = S bonds during the strong interaction with the nucleophilic O atoms of H_2O.[22] As higher levels of TAA facilitated the release rate of S^{2-}, larger crystals could be formed and then assembled into NPs with rougher surfaces.[8] However, a certain excess of TAA may restrain the further growth of ZnS NPs,[15] leading to the obvious reduction in size, as displayed in Figure 3D.

2.1.2. ZnS–CdS Nanocomposites

As shown in **Figure 4**, the ZnS–CdS nanocomposites (NCs) exhibit significantly different features in the XRD pattern, compared with pure ZnS NPs, with three new peaks at 26.53°,

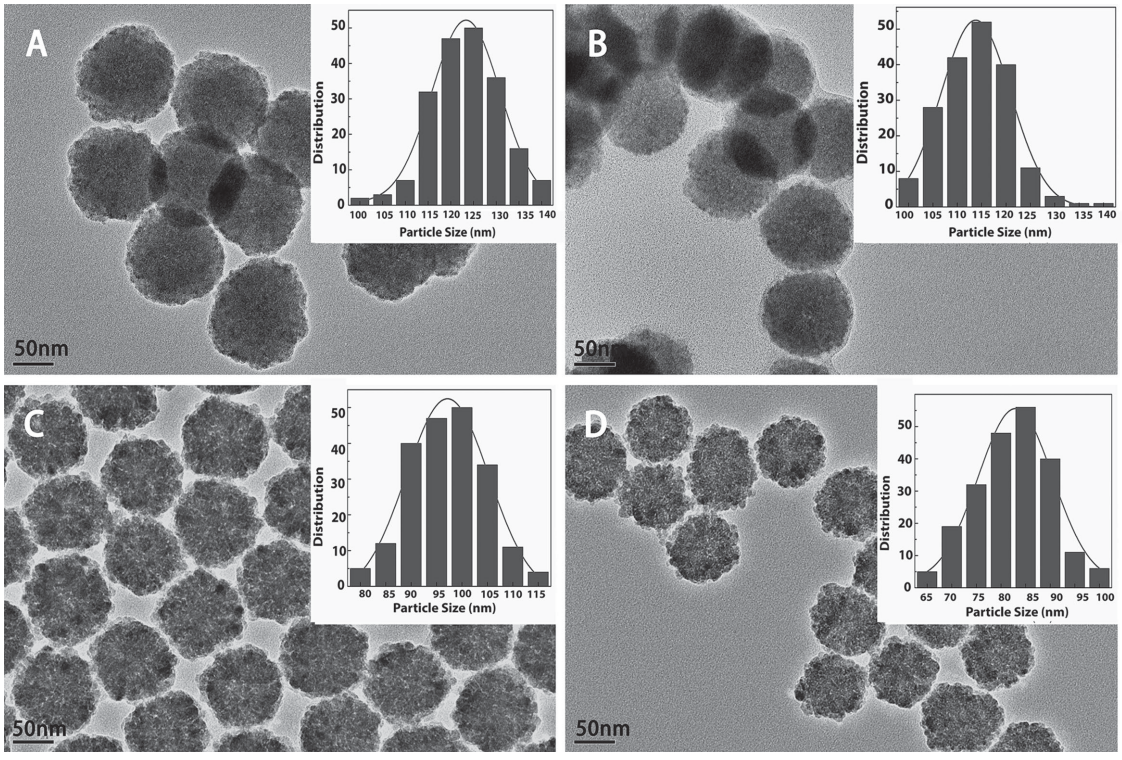

Figure 3. TEM images of pure ZnS NPs synthesized at different molar ratios of $Zn(Ac)_2$ to TAA at 100°C for 2 h: A) 1:1, B) 1:5, C) 1:10, and D) 1:17, respectively. The inset of each image shows the corresponding particle size distribution.

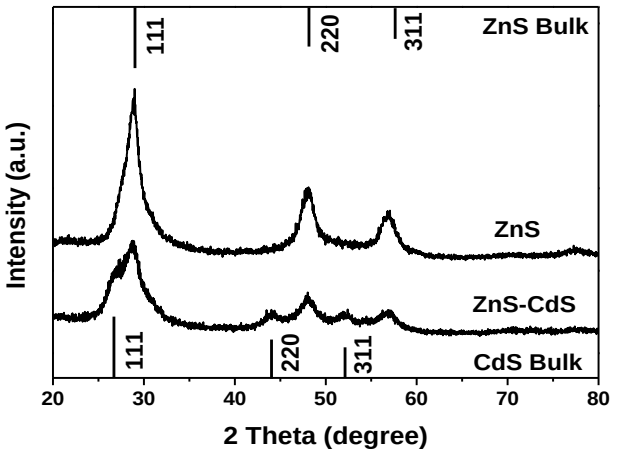

Figure 4. XRD patterns of the pure ZnS NPs, synthesized at the molar ratio of $Zn(Ac)_2$: TAA = 1:10, and the ZnS–CdS NCs.

44.01° and 52.08°, which can be easily indexed to cubic CdS structure (JCPDS Card No. 75–1546). One can notice that the bottom XRD pattern was composed of two sets of diffraction peaks (Cubic ZnS and Cubic CdS), which indicates the successful decoration of tiny CdS nanoparticles onto ZnS cores. No other characteristic peaks of impurities are observed, demonstrating the high quality of as-synthesized products. Besides, it is observed that the peak intensity of ZnS–CdS was weaker than that of pure ZnS, resulting from the shield of CdS layer against the incoming X-ray.[23]

After the attachment of tiny CdS NPs, the white powder turned bright yellow. The SEM images of ZnS NPs and ZnS–CdS NCs are depicted in **Figure 5**A,B. Both the ZnS NPs before and after coating were uniform, except for the difference in surface roughness. In contrast to the spherical ZnS NPs, the flower-like appearances of ZnS–CdS NCs indicate the successful assemblies of tiny CdS NPs onto the surface of ZnS cores (as shown in the inset of Figure 5B). Further investigations of structure and morphology have been performed through TEM and HRTEM, as discussed below.

In comparison, it is evident that ZnS NPs were decorated with a new layer, judging from the contrast of brightness between the inner and exterior layer of the NPs, as displayed in the TEM images of ZnS NPs and ZnS–CdS NCs in **Figure 6**B,E. The slight increase in particle sizes, calculated from the statistics collected in the inset of Figure 6A,D, further implies the formation of tiny CdS NPs onto ZnS cores, which can be more distinctly recognised in Figure 6C,F. The successful attachment of CdS NPs of 8–10 nm caused the surfaces of the as-formed NCs to roughen. With a careful observation of Figure 6C, the lattice constant of the ZnS NPs was affirmed to be about 0.302 nm, which corresponded to the (111) plane of bulk blende ZnS. The HRTEM image of tiny CdS NPs (Figure 6F) shows 0.331 nm and 0.213 nm interlayer lattice spacings, where the CdS phase matched well with the (111) and (220) planes of bulk cubic CdS. The crystal structure consistent with the XRD patterns indicates the polycrystalline nature of the as-formed ZnS–CdS NCs. The oriented self-assembly growth mechanism based on aggregation was thus further verified by these measurements and observations.

2.2. Consitutent Study

A detailed chemical analysis of ZnS and ZnS–CdS samples was carried out through elemental mappings and EDS measurement. **Figure 7**A depicts a typical TEM image of pure ZnS NPs. Meanwhile, the corresponding EDS mappings in Figure 7B,C demonstrates the distribution of the constituting elements, S and Zn, revealing the homogeneity across the particles. The EDS spectra in Figure 7D agrees with the results of the elemental mappings. While the intense signals of C and Cu came from the copper tent substrate, no other elements of impurities were detected, suggesting the high quality of the as-synthesized products.

Figure 8A shows a typical TEM image of the ZnS–CdS NCs and Figure 8B–D illustrates the distribution of the elements, S, Zn, and Cd. The loose and uniform distribution of element Cd, as displayed in Figure 8D, demonstrates that tiny CdS NPs spread discretely and uniformly on the surfaces of ZnS NPs. The expected characteristics of the constituents were in accordance with the results from EDS spectra in Figure 8E. However, the element O came from the partial oxidation of ZnS–CdS by the oxygen in air.[14]

2.3. Growth Mechanism

The growth mechanism of ZnS NPs and ZnS-CdS NCs is illustrated in **Scheme 1**. For the first part of this experiment, PVP played an indispensable role in the formation of ZnS NPs and the narrow distribution of NPs, whereas only floccus was observed in the absence of surfactant PVP. The capping agent PVP, with a structure of polyvinyl skeleton, served two roles in the reaction process: a) it prevented the further growth of particles by creating the passivation layer around ZnS cores through the strong interaction with Zn^{2+} and O, N atoms of the pyrrolidon ring;[22,24] b) it prohibited the agglomeration of ZnS NPs through the nature of the repulsive forces among the polyvinyl groups.[6,25] The morphology and size of ZnS samples could be easily attuned by adjusting the initial

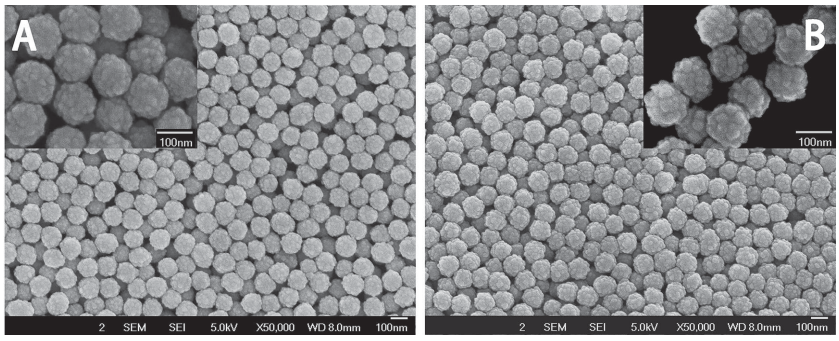

Figure 5. SEM images of A) the pure ZnS NPs, synthesized at the molar ratio of $Zn(Ac)_2$:TAA = 1:10, and B) ZnS–CdS NCs.

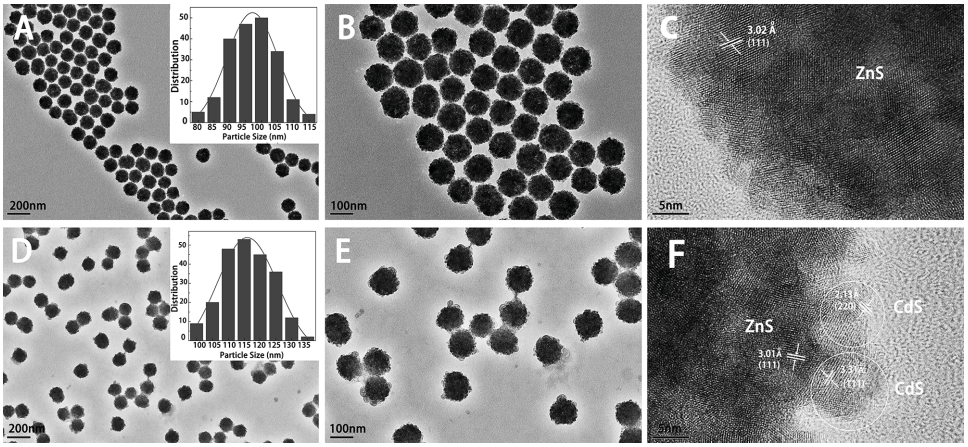

Figure 6. A,B) TEM images and C) HRTEM image of pure ZnS NPs synthesized at the molar ratio of $Zn(Ac)_2$:TAA = 1:10; D,E) TEM images and F) HRTEM image of ZnS–CdS NCs. The inset of (A,C) reveals the corresponding particle size distribution.

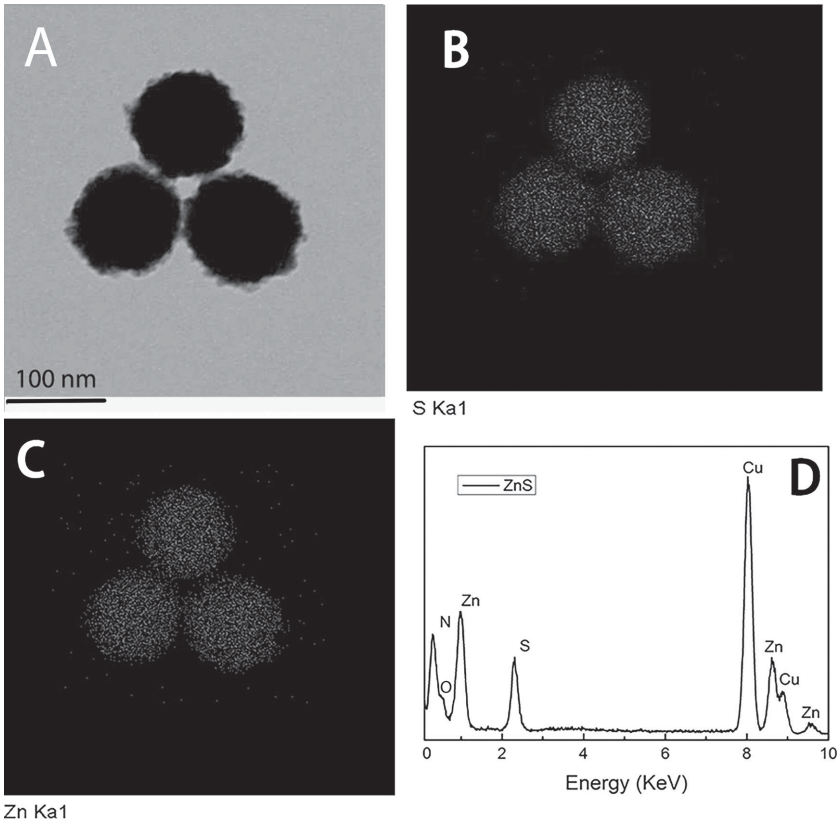

Figure 7. A) Typical TEM image of pure ZnS NPs synthesized at the molar ratio of $Zn(Ac)_2$:TAA = 1:10; B,C) The elemental maps of S and Zn revealing well-defined constituent distributions within the nanoparticle; D) The corresponding EDS spectra of ZnS NPs.

concentration of TAA. For example, when the starting ratio of $Zn(AC)_2$ to TAA was increased from 1:1 to 1:5 or 1:10, the surface morphology turned rougher despite the size similarities. However, when the amount of TAA reached a certain level, for example, the starting ratio of $Zn(AC)_2$ to TAA being 1:17, ZnS NPs with a remarkably reduced size could be obtained. The reaction mechanism was proposed as follows. H_2S would be released from TAA in the aqueous solution when heated to 100 °C. Then Zn^{2+} ions would react with S^{2-} ions to form ZnS tiny nanocrystals. Higher concentration of TAA which favored prompt release of H_2S contributed to the faster nucleation and growth of ZnS crystals, during which the crystal grains of larger sizes were more likely to be produced.[26] To minimize the surface energy, these nanocrystals then self assembled steadily into spherical structures via the oriented self-aggregation.[21] As a result, the ZnS NPs composed of bigger crystal grains revealed greater coarseness. With regard to the extremely large excess of TAA, as of the case of $C_{Zn(AC)2}$:C_{TAA} = 1:17, it was the tradeoff effect between the Zn^{2+} ions on the surface of the synthesized NCs and the redundant TAA that restrained the sizes of ZnS NPs.[8]

For the coating of ZnS cores, Cd^{2+} ions would attach to the surface of ZnS NPs spontaneously through electrostatic attraction, as the surface charge of ZnS NPs was negative in aquatic solutions according to ú-potential measurement, which was consistent with the result in Wang's work.[27] Therefore, the ZnS NPs acted as the centers for lateral deposition of tiny CdS NPs after the introduction of S^{2-} ions into the system.[28] Subsequently, the high-productivity ZnS NPs modified with tiny CdS NPs could be obtained through the nucleation and growth process. The detailed reaction processes were described in the following chemical equations.[18]

$$CH_3CSNH_2 + 2H_2O \rightarrow H_2S + CH_3COOH + NH_3 \quad (1)$$

$$Zn^{2+} + S^{2-} \rightarrow ZnS \quad (2)$$

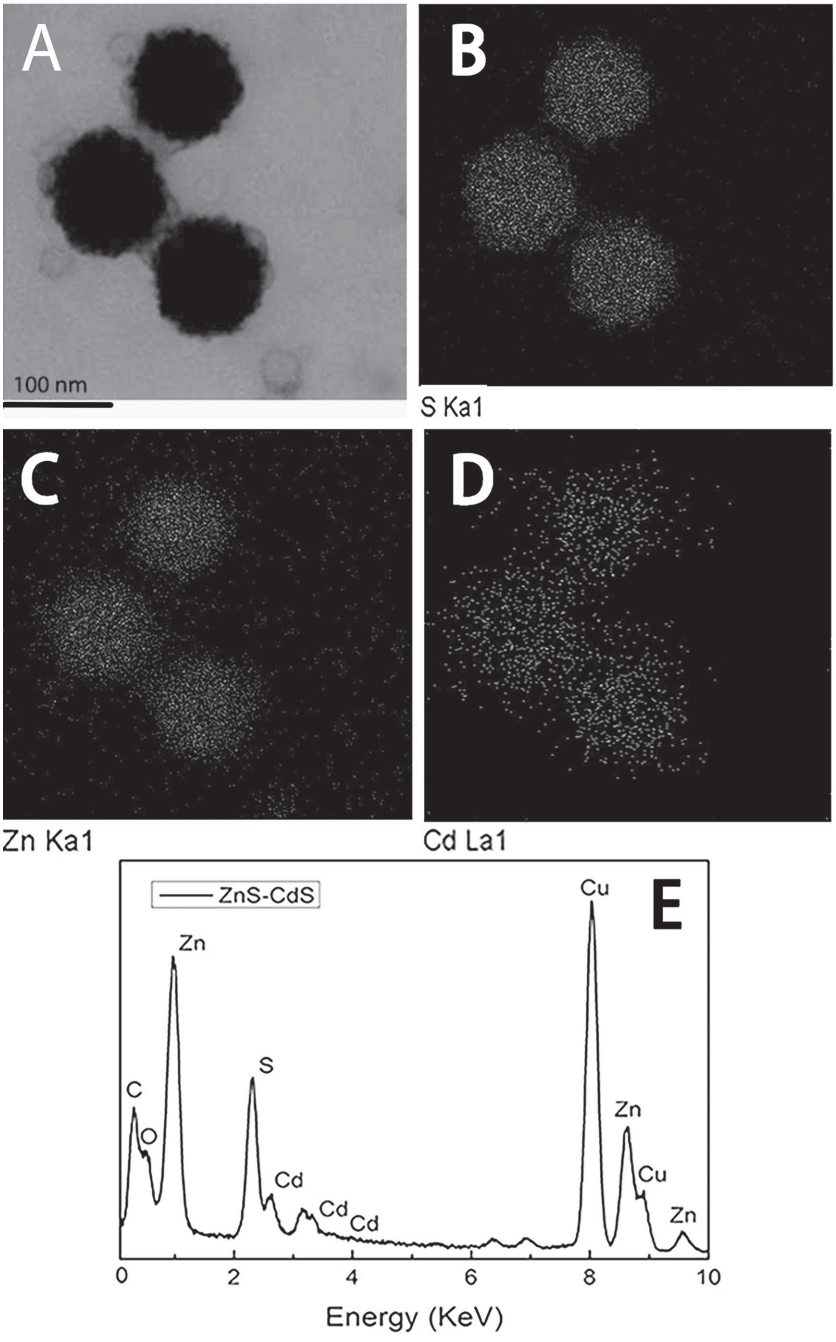

Figure 8. A) Typical TEM image of ZnS–CdS NCs; B–D) The elemental maps of S, Zn, and Cd revealing well-defined constituent distributions within the nanocomposite; E) The EDS spectra of ZnS–CdS NCs.

$$CH_3CSNH_2 + 2H_2O \rightarrow H_2S + CH_3COOH + NH_3 \quad (3)$$

$$Cd^{2+} + S^{2-} \rightarrow CdS \quad (4)$$

2.4. Optical Properties

The UV–Vis spectrums of the as-prepared ZnS NPs at different levels of TAA and ZnS–CdS NCs are shown in **Figure 9**A. A broad absorption peak centered at about 234 nm and a shoulder peak at 347 nm were observed of all the ZnS samples, revealing a great blue shift in contrast to the bulk ZnS due to quantum size effect.[21] A fair enhancement of the photo-absorption intensity of the ZnS NPs in the range of 200–350 nm could be noticed with the increase of TAA concentration. However, after being decorated with tiny CdS NPs, there occurred a slight red shift of absorption peaks compared with the pure ZnS products. There were 3 possible reasons responsible for phenomenon: a) The delocalization of the electronic wave function resulting from the indirect spatial nature of excition and large transition energy variations after the attachment of CdS;[29] b) The decreased potential well effect caused by the relatively lower band gap of CdS;[30] c) The extended photoresponse range, which came from CdS with the bandgap of 2.4 eV, accounted for the red shift as well.[31] These above mentioned subjects are prone to have an effect on the electronic states and absorption properties.[19] Moreover, it is noticeable that the absorption intensity of the ZnS–CdS NCs was greatly promoted after the deposition of tiny CdS NPs.

The photoluminescence (PL) intensities of the products under the excitation light of 290 nm are displayed in Figure 9B. It is obvious that all the curves had almost the same PL band positions, including a relatively strong one centered at 467 nm and a weaker one centered at about 390 nm. Similar to the previously reported result, the broad violet emission centered around 380–400 nm came from the interstitial Zn defects or dislocations.[30] The stable and relatively strong blue emission peak at 467 nm may be ascribed to the luminescence originated from the sulfur vacancies.[32] Since the donor states produced by sulfur vacancies is lower than conduction band, there exerts a potential in the localized charge. Thus, the electrons tend to migrate from sulfur vacancies to the conduction band during the excitation process. Whenever a captured electron recombines with a hole in the interstitial sulfur states instead of the valance band, there may occur the blue emission at about 480nm.[32] When comparing ZnS–CdS NCs with pure ZnS samples, it appears that the CdS played an important role in the PL intensity rather than peak position. There was no significant PL peak from CdS, which may be ascribed to the relatively small amount of CdS in the NCs. Interestingly, the PL intensity of ZnS–CdS NCs was drastically improved when measured under the same conditions. Two explanations were proposed for the enhancement of PL

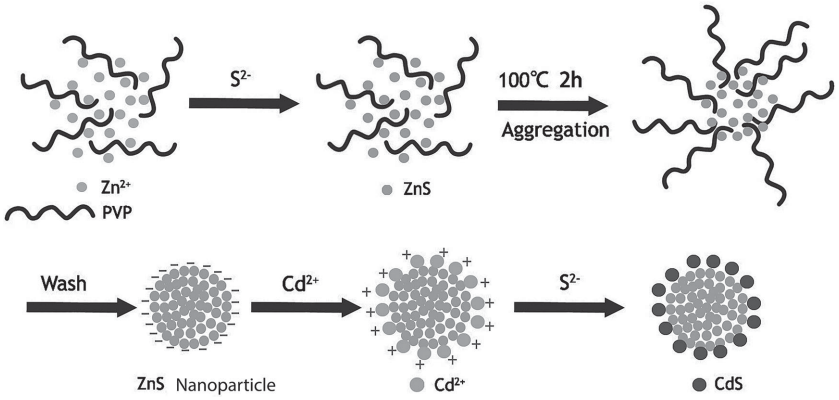

Scheme 1. Schematic illustration of growth mechanism of the ZnS–CdS NCs.

intensity after the attachment of tiny CdS NPs: a) Owning to the band-gap structure of ZnS and CdS, the tunneling of charge carriers might be suppressed by the CdS, which meant more photogenerated electrons and holes would be trapped inside the ZnS cores, resulting in the enhancement of radiative transitions;[23] b) After the attachment of CdS particles, the number of electron capture centers on the surface of ZnS NPs would be greatly reduced, which also prompted the increase of PL intensity.[23,34] However, the detailed optical properties for the ZnS series are yet to be further investigated.

2.5. Photocatalytic Activity

To understand the potential applications of as-prepared ZnS NPs and ZnS–CdS NCs, the photocatalytic performances of as-obtained samples were evaluated by degrading Rhodamine B (RhB, initial concentration: 20 mg/L) under UV light (100 W) for a given time. **Figure 10** indicates the decrease of the main absorption peak intensity of RhB in the presence of various ZnS catalysts. $(C_0–C)/C_0$ stands for the degradation rate of organic dyes, where C is the concentration of RhB at each irradiated time, and C_0 is the initial concentration when adsorption–desorption equilibrium is achieved. Interestingly, ZnS NPs prepared at the starting ratio of $C_{Zn(Ac)2}$:C_{TAA} = 1:1 displayed a poor photocatalytic activity, while the degradation rate was greatly improved with the increase of the initial TAA level, as shown in Figure 10D. After being exposed to the UV light for 60 min, 81% of RhB was decomposed with the assistance of the ZnS NPs catalyst prepared at the starting ratio of $C_{Zn(Ac)2}$:C_{TAA} = 1:10. Meanwhile, it only reached 22%, 36% and 45% at the starting ratios of 1:1, 1:5, 1:17, respectively. The differences in photoactivity among the ZnS samples could be ascribed to two crucial factors. Firstly, the increased specific surface area induced by surface coarseness when the TAA amount was raised, as discussed before, created new surface facets, which served as reaction centers.[35,36] Secondly, the enhanced crystallinity with the increase of the S source, as depicted in XRD patterns of Figure 1, favored effective separations of photogenerated electrons and holes through reducing lattices defects which acted as the recombination centers for charge carriers.[5,20] However, as for the ZnS sample with the ratio of 1:17, despite the reduced sizes, the defects brought about by the large excess of TAA might hinder the charge transport, resulting in the relatively weak photocatalytic performance. Therefore, the ensuing work was focused on the ZnS NPs samples with the ratio of 1:10 which showed the highest photodegradation rate.

Further comparison of the photocatalytic activities of pure ZnS NPs and ZnS–CdS NCs is shown in **Figure 11**. It is evident that the ZnS–CdS NCs exhibited higher photocatalytic activities than pure ZnS NPs. Quantitatively, up to 50% RhB was decomposed within 10 min in the presence of the ZnS–CdS catalysts, about three times as much as that decomposed by pure ZnS NPs, and twice as much as that decomposed by pure CdS NPs synthesized under the previously reported strategy by Yang et al.[35] After all, it only took 30 min, for ZnS–CdS NCs, to degrade 92% RhB, much faster than the commercial ZnS powder. With a closer observation, a fair blue shift in the photodegradation process of RhB in Figure 11B was revealed of the ZnS–CdS NCs, while no obvious change occurred of pure ZnS samples. Indeed, the photocatalytic decomposition of RhB was a complicated process involving N-demethylation and the destruction of the conjugated structure.[37] The diminishing of absorption peak at 500 nm came from the direct degradation of chromophoric groups in RhB into small organic molecules, or CO_2 and H_2O, while the blue shift was related to the formation of de-ethylated RhB molecules.[36] Therefore, after the degradation process, the RhB turned transparent for the ZnS samples and light yellow for the ZnS–CdS nanoscomposites, respectively. To further understand the above results, **Scheme 2** was employed to depict the photodegradation process in the presence of ZnS–CdS NCs towards RhB. There was no obvious potential barrier existing at the interface of ZnS–CdS,

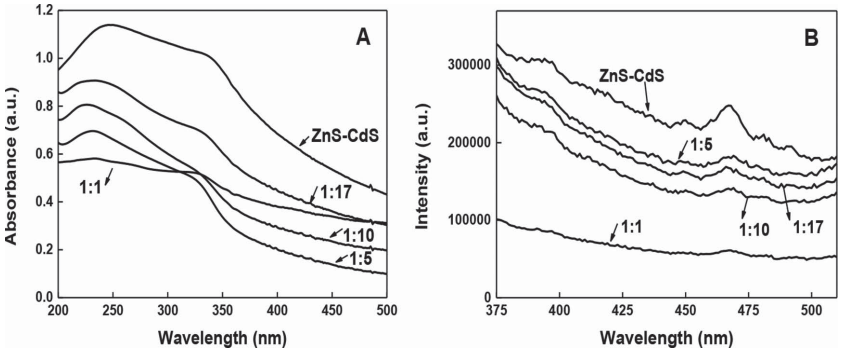

Figure 9. A) UV–Vis spectrum and B) room-temperature PL spectrum of the ZnS NPs synthesized at different molar ratios of $Zn(Ac)_2$ to TAA, 1:1, 1:5, 1:10, and 1:17, respectively, and the ZnS–CdS NCs (as indicated).

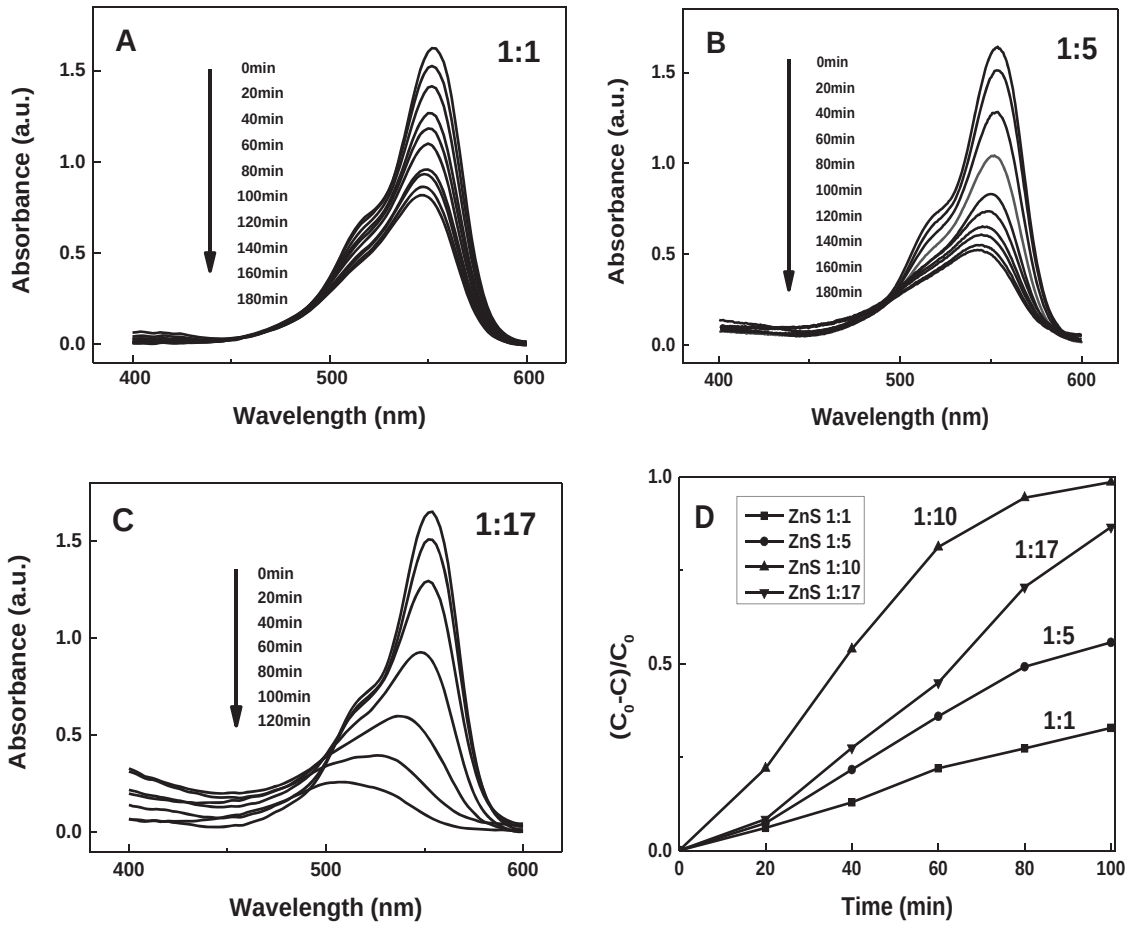

Figure 10. UV–Vis absorption spectral changes for RhB as a function of irradiation time in the presence of pure ZnS NPs prepared at different molar ratios of $Zn(Ac)_2$ to TAA: A) 1:1, B) 1:5, C) 1:17; D) The corresponding photodegradation rate of RhB in the presence of ZnS NPs prepared at different molar ratios of $Zn(Ac)_2$ to TAA.

as the discrete CdS layer was too thin to afford an interfacial depletion layer. Therefore, the photogenerated electrons could migrate easily from CdS to ZnS by means of ballistic diffusion.[38] When exposed to UV light, the electrons in the valence band (VB) of semiconductors could be excited to the conduction band (CB), while the same amount of holes remained in the VB, which was applicable for both ZnS and CdS here. However, the photogenerated electrons in the CB of CdS would diffuse into the CB of ZnS to achieve a balance in Fermi energy level equilibration due to the higher electron affinity of CdS.[9,39] Meanwhile, driven by potential energy, the photogenerated holes transferred from the VB of ZnS to that of CdS, during which more active charges would participate in the degradation process as a result of better charge separation and prolonged lifetime for photogenerated electrons and holes.[40,41] Afterwards, the holes localized in the VB of CdS would react with OH^- to form powerful oxidant hydroxy radicals ·OH, which would decompose the organic dye. The electrons left in the CB of ZnS would reduce the O_2 absorbed on the surface into superoxide anion radicals O^{2-}, which in turn produced ·OH.[16,33,42] In this manner, the photocatalytic performance of ZnS NPs was significantly enhanced by the surface modification with tiny CdS NPs.

3. Conclusion

A facile two-step solution-phase route to synthesize highly uniform colloidal ZnS–CdS NCs is proposed in this paper. The successful attachment of tiny CdS NPs onto the surface of ZnS NPs, which can be obtained in aqueous solutions, greatly enhances the photodegradation activities compared with pure ZnS NPs. The coupling effect of ZnS–CdS NCs is also investigated through PL spectra which also shows a remarkable improvement relative to plain ZnS NPs. Furthermore, it is noticed that the surface roughness and particle sizes of ZnS NPs can be tuned by adjusting the proportion of the S source via the aqueous solution method. Especially, the ZnS NPs prepared at the starting ratio of $Zn(AC)_2$ to TAA = 1:10 exhibit higher photocatalytic activities than any other as-synthesized ZnS samples and commerical ZnS powers. The strategy presented in our work is expected to offer exciting opportunities not only for fundamental growth mechnism of nanostructures, but also for the design of new heterostructured semiconductor hybrids, such as ZnS/CuS and ZnS/CdSe. Moreover, the excellent photocatalytic performance of ZnS–CdS NCs indicates the great application potentials in photocatalysis and optoelectronics.

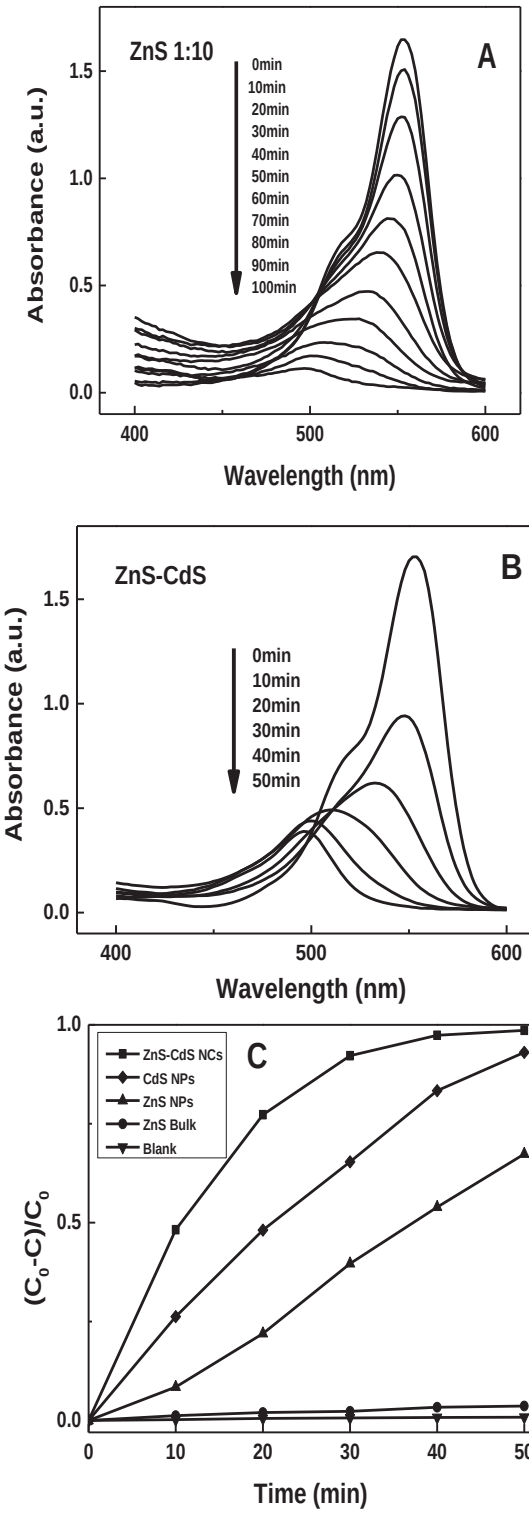

Figure 11. UV–Vis absorption spectral changes for RhB as a function of irradiation time in the presence of A) pure ZnS NPs synthesized at the molar ratio of $Zn(Ac)_2$ to TAA = 1:10 and B) ZnS–CdS NCs; C) The corresponding photodegradation rate of RhB in the presence of ZnS NPs(1:10) and ZnS–CdS NCs. The commerical ZnS powders and pure CdS NCs were also included for comparison.

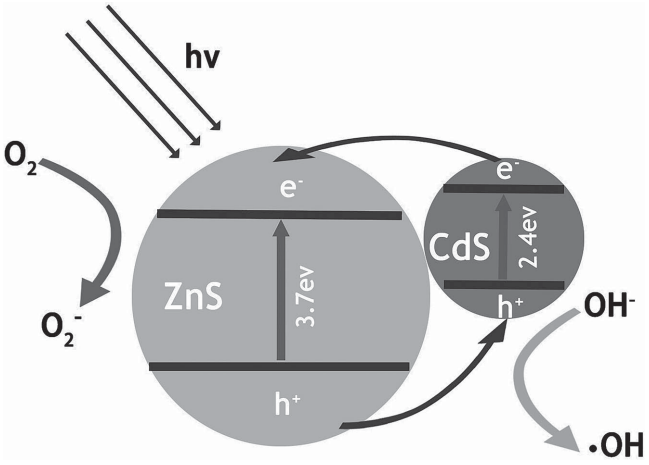

Scheme 2. Schematic illustration of the photocatalytic mechanism of as-synthesized ZnS–CdS NCs.

4. Experimental Section

Preparation of ZnS NPs: All chemicals, purchased from Sinopharm Chemical Reagent Corp, were of analytical reagent grade and directly used without any further treatment. In a typical procedure which is similar to Zhang's work,[21] $Zn(COOH)_2$ ($Zn(AC)_2$, 4 mmol, 0.732 g) and surfactant PVP (2 g) were dissolved in 400 ml of de-ionized water and stirred up for 15 min to form a clear solution. Meanwhile, CH_3CSNH_2 (TAA, 4 mmol, 0.3 g) was added into a glass beaker containing 200 ml of de-ionized water and stirred for 15 min before added into the clear solution of $Zn(AC)_2$ and PVP. Subsequently, the conical flask containing the mixtured solution was kept in an oil bath at 100 °C for 2 h under continuously stirring and cooled down naturally to room temperature. Then the products were collected by centrifugation and washed with distilled water and absolute ethanol for several times. The final products were dried in a vacuum oven at 60 °C for 3 h. Different ZnS NPs were obtained by adjusting the starting ratio of $C_{Zn(Ac)2}$:C_{TAA} to 1:5, 1:10 and 1:17, respectively. The ZnS samples which were prepared at the $C_{Zn(Ac)2}$:C_{TAA} = 1:10 were selected for further experiment.

Preparation of ZnS–CdS NCs: Inspired by Liu's work,[18] the as-synthesized ZnS NPs (1 mmol) and $Cd(NO_3)_2{\cdot}4H_2O$ (1 mmol) were dissolved in 50 mL of de-ionized water to form a clear solution, followed by the addition of TAA (1 mmol). Afterwards, the mixture was stirred up for 30 min and transferred to a conical flask. It was kept in an oil bath at 80 °C for 1 h under vigorously stirring and then cooled down naturally to room temperature. After being washed with distilled water and absolute ethanol for several times, the yellow precipitates were obtained and subsequently dried in a vacuum oven at 60 °C for 3 h.

Preparation of CdS NCs: For comparison, the pure CdS NCs with the similar sizes of ZnS NPs were prepared using Yang's method.[35] $Cd(NO_3)_2{\cdot}4H_2O$ (2 mmol, 0.62 g) and PVP (2 g) were dissolved in the mixed solvent of ethanol/H_2O (v:v = 2:3) and stirred for 30 min. Meanwhile, 0.75 g TAA was dissolved in the same solvent (100 mL) and added into the former solution. Afterwards, $NH_3{\cdot}H_2O$ (v:v = 1:1) was added dropwise into the solution. After being incubated at room temperature for 1 h, the yellow precipitates were centrifuged and washed with distilled water and absolute ethanol for several times. The final products were dried in a vacuum oven at 60 °C for 3 h.

Photocatalytic Performance Measurement: The photocatalytic performance was evaluated through the decomposition of RhB (Rhodamine B, 50 ml, 20 mg/L) under ultraviolet irradiation (100 w) at room temperature in the presence of photocatalyst (100 mg). After being stirred in the dark for 30 min to achieve the absorption-desorption equilibrium, the mixture was exposed to the UV light under

constant stirring. For a given duration (such as 10 min), the change in the concentration of RhB (after the removal of photocatalysts through centrifugation) was recorded by the UV–Visible spectrophotometer (Hitachi U-4100).

Charaterization: X-ray diffraction using Cu Kα radiation (XRD, Bruker D8-A25) was adopted for studying the structure of the samples. Field-emission scanning electron microscopy (FESEM, JSM-6701F) and transmission electron microscopy accompanied with EDS and EDS Mapping (TEM, CM200FEG) were employed to analyze the morphology and composition of all the products. The optical properties of the samples were characterized using a UV–Vis spectrophotometer (Hitachi U-4100). The fluorescence performance of the samples at room-temperature were characterized via the photoluminescence (PL) spectro-fluorometer (Fluoromax-4), where the 290-nm light was induced from a He-Cd laser source to excite the samples.

Acknowledgements

The authors appreciate the kind support from Prof. Ziqi Liang from Fudan for the PL experimental measurements. The work was supported by the National Natural Science Foundation of China (Grant Nos. 51471051 and 51372040), Science and Technology Commission of Shanghai Municipality (13NM1400300), Shanghai Shu Guang Project (12SG01), Innovation Program of Shanghai Municipal Education Commission (14ZZ003), the Programs for Professor of Special Appointment (Eastern Scholar) at Shanghai Institutions of Higher Learning. The work was partially supported by the Deanship of Scientific Research, King Abdulaziz University under grant No. (47–130–35-HiCi).

Received: September 5, 2014
Revised: October 19, 2014
Published online: November 11, 2014

[1] M. Y. Liao, S. Hishita, E. Watanabe, S. Koizumi, Y. Koide, *Adv. Mater.* **2010**, *22*, 5393.
[2] a) L. Peng, L. F. Hu, X. S. Fang, *Adv. Mater.* **2013**, *25*, 5321; b) H. Liu, Z. M. Zhang, L. F. Hu, N. Gao, L. W. Sang, M. Y. Liao, R. Z. Ma, F. F. Xu, X. S. Fang, *Adv. Opt. Mater.* **2014**, *2*, 771.
[3] a) H. Q. Wang, L. C. Jia, P. Bogdanoff, S. Fiechter, H. Moehwald, D. Shchukin, *Energy Environ. Sci.* **2013**, *6*, 799; b) W. W. Zhou, C. W. Cheng, J. P. Liu, Y. Y. Tay, J. Jiang, X. T. Jia, J. X. Zhang, H. Gong, H. H. Hng, T. Yu, H. J. Fan, *Adv. Funct. Mater.* **2011**, *21*, 2439.
[4] a) X. S. Fang, C. H. Ye, L. D. Zhang, Y. H. Wang, Y. C. Wu, *Adv. Funct. Mater.* **2005**, *15*, 63; b) Z. X. Wang, L. M. Wu, M. Chen, S. X. Zhou, *J. Am. Chem. Soc.* **2009**, *131*, 11276.
[5] X. S. Fang, T. Zhai, U. K. Gautam, L. Wu, Y. Bando, D. Golberg, *Prog. Mater. Sci.* **2011**, *56*, 175.
[6] a) S. Xiong, B. Xi, C. Wang, D. Xu, Z. Zhu, Y. Qian, *Adv. Funct. Mater.* **2007**, *17*, 2728; b) J. Hu, L. Ren, Y. Guo, H. Liang, A. Cao, L. Wan, C. Bai, *Angew. Chem.* **2005**, *117*, 1295.
[7] D. Chen, F. Huang, G. Ren, D. Li, Y. Wang, L. Zhang, *Nanoscale* **2010**, *2*, 2062.
[8] M. Mohammadikish, F. Davar, M. R. Loghman-Estarki, *J. Clust. Sci.* **2013**, *24*, 217.
[9] T. K. Jana, A. Pal, K. Chatterjee, *J. Alloy. Compd.* **2014**, *583*, 510.
[10] M. R. Kim, Y. Kang, D. Jang, *J. Phys. Chem. C* **2007**, *111*, 18507.
[11] Y. P. Xie, Z. B. Yu, G. Liu, X. L. Ma, H. Cheng, *Energy Environ. Sci.* **2014**, *7*, 1895.
[12] D. V. Talapin, A. L. Rogach, M. Haase, H. Weller, *Nano. Lett.* **2001**, *1*, 207.
[13] X. Peng, M. C. Schlamp, A. V. Kadavanich, A. P. Alivisatos, *J. Am. Chem. Soc.* **1997**, *119*, 7019.
[14] J. Yan, X. S. Fang, L. Zhang, U. K. Gautam, T. Sekiguchi, D. Golberg, *Nano. Lett.* **2008**, *8*, 2794.
[15] S. C. Han, L. Hu, N. Gao, A. A. Al-Ghamdi, X. S. Fang, *Adv. Funct. Mater.* **2014**, *24*, 3725.
[16] L Wang, H. Wei, Y. Fan, X. Liu, J. Zhan, *Nanoscale Res. Lett.* **2009**, *4*, 558.
[17] Y. J. Hsu, S. Y. Lu, Y. F. Lin, *Adv. Funct. Mater.* **2005**, *15*, 1350.
[18] S. Liu, H. Li, L. Yan, *Mater. Res. Bull.* **2013**, *48*, 3328.
[19] X. Q. Meng, D. X. Zhao, X. W. Fan, X. H. Wang, *Mater. Lett.* **2007**, *61*, 3535.
[20] H. Zhang, X. Chen, Z. Li, J. Kou, T. Yu, Z. Zou, *J. Phys. D: Appl. Phys.* **2007**, *40*, 6846.
[21] Y. Li, Q. Li, H. Wu, M. Nie, Y. Zhang, *Mater. Sci. Eng. B* **2013**, *178*, 135.
[22] L. Wang, X. Tao, J. Yang, Y. Ren, Z. Liu, M. Jiang, *Opt. Mater.* **2006**, *28*, 1080.
[23] D. Chen, F. Zhao, H. Qi, M. Rutherford, X. Peng, *Chem. Mater.* **2010**, *22*, 1437.
[24] G. Ghosh, M. Kanti Naskar, A. Patra, M. Chatterjee, *Opt. Mater.* **2006**, *28*, 1047.
[25] R. He, X. Qian, J. Yin, H. Xi, L. Bian, Z. Zhu, *Colloid Surf. A-Physicochem. Eng. Asp.* **2003**, *220*, 151.
[26] F. Gu, C. Z. Li, S. F. Wang, M. K. Lü, *Langmuir* **2006**, *22*, 1329.
[27] C. S. Lao, M. Park, D. L. Polla, Z. L. Wang, *J. Am. Chem. Soc.* **2007**, *129*, 12096.
[28] J. Geng, X. Jia, J. Zhu, *CrystEngComm* **2010**, *13*, 193.
[29] F. Xu, V. Volkov, Y. Zhu, X. Gao, I. L. Kuskovsky, H. Matsui, *J. Phys. Chem. C* **2009**, *113*, 19419.
[30] M. Sookhakian, Y. M. Amin, W. J. Basirun, N. Kamarulzaman, *J. Lumin* **2014**, *145*, 244.
[31] Z. Zeng, C. S. Garoufalis, A. F. Terzis, S. Baskoutas, *J. Appl. Phys.* **2013**, *114*, 23510.
[32] N. Gupta, B. Pal, *Chem. Eng. J.* **2014**, *246*, 260.
[33] M. Ethayaraja, C. Ravikumar, K. Dutta, R. Bandyopadhyaya, *J. Phys. Chem. C* **2007**, *111*, 3246.
[34] Q. Yang, H. Cai, Z. Hu, Z. Duan, X. Yang, J. Wu, *Nanoscale Res. Lett.* **2014**, *9*, 31.
[35] Y. Guo, J. Wang, Z. Tao, P. Hu, Y. Xu, L. Yang, *CrystEngComm* **2012**, *14*, 1185.
[36] E. G. L. Oliveira, J. J. Rodrigues, H. P. de Oliveira, *Chem. Eng. J.* **2011**, *172*, 96.
[37] J. Li, X. Zhang, Z. Ai, F. Jia, L. Zhang, J. Lin, *J. Phys. Chem. C* **2007**, *111*, 6832.
[38] J. Nayak, H. Lohani, T. K. Bera, *Curr. Appl. Phys.* **2011**, *11*, 93.
[39] M. Zirak, O. Moradlou, Y. T. Nien, A. Z. Moshfegh, *Appl. Surf. Sci.* **2013**, *273*, 391.
[40] G. Guerguerian, F. Elhordoy, J. R. Ramos-Barrado, E. A. Dalchiele, *Nanotechnology* **2011**, *22*, 505401.
[41] O. Amiri, H. Emadi, S. S. Mostafa Hosseinpour-Mashkani, M. Sabet, M. M. Rad, *RSC Adv.* **2014**, *4*, 10990.
[42] P. Praus, L. Svoboda, J. Tokarský, A. Hospodková, V. Klemm, *Appl. Surf. Sci.* **2014**, *292*, 813.